AIMS Bioengineering

AIMS Bioengineering, 12(2): 225–248.
DOI: 10.3934/bioeng.2025011
Received: 24 February 2025
Revised: 15 April 2025
Accepted: 16 May 2025
Published: 29 May 2025

https://www.aimspress.com/journal/Bioengineering

Research article

Influence of white pigment on the properties of polylactic acid scaffolds for 3D printing: in vitro and in vivo analysis

Mariana Nataly Carbajal-Casique[1], Lucía Pérez-Sánchez[1,*], Marco Antonio Alvarez-Perez[1], Gerardo Daniel Rayo-López[2], Jorge-Alejandro Reyes-Esqueda[2], Francisco Marichi-Rodríguez[1] and Janeth Serrano Bello[1,*]

[1] Tissue Bioengineering Laboratory, Division of Graduate Studies and Research, Faculty of Dentistry, National Autonomous University of Mexico, Exterior Circuit no/#. University city, 04510 Coyoacán, Mexico City, Mexico

[2] University Laboratory of Surface Optics, Solid State, Institute of Physics, UNAM, Scientific Research, University City, Coyoacán, 04510, Mexico City, Mexico

Correspondence: Email: janserbello@fo.odonto.unam.mx; luciaperez@fo.odonto.unam.mx.

Abstract: Polylactic acid (PLA) is a widely used polymer in tissue engineering due to its biocompatibility, biodegradability, and easy processing. However, to this day, white and translucent PLA are used indistinctly in the field though there are several studies that establish changes in the materials properties in the presence or absence of pigments. Here, we proposed an in vitro and in vivo methodology with 3D-printed scaffolds to further examine how their surface structure and cellular response vary. We observed surface structure, pore size, and porosity, and conducted in vitro cell assays. In vivo, male Wistar rats were used to collect histological samples and analyze the inflammatory response. DS revealed that the translucent scaffold contained 61.37 ± 3.96 wt% carbon and 38.64 ± 3.95 wt% oxygen and measured 8.96 ± 0.85 mm in diameter and 0.97 ± 0.3 mm in width, while the white scaffold showed 56.28 ± 1.82 wt% carbon and 43.66 ± 1.92 wt% oxygen and measured a diameter of 9.15 ± 0.56 mm and width of 1.01 ± 0.2 mm. The white PLA scaffold showed better structure and 67% porosity with larger pores compared to the translucent scaffold, which had 53% porosity and smaller pores. Both types were accepted by fetal osteoblast cells, but the translucent scaffold was associated with large foreign-body cells. Moreover, PLA's pigment increases surface tension, which helps the material maintain its shape as it cools and produces a better surface structure.

Keywords: white pigment; translucent pigment; 3D printed scaffolds; tissue engineering; PLA

1. Introduction

Polylactic acid (PLA) is a widely utilized synthetic polymer in bone tissue engineering due to its favorable properties, such as biodegradability, biocompatibility, and easy processing. PLA scaffolds can be fabricated using techniques like 3D printing, enabling precise control over architecture, porosity, and mechanical strength [1–3]. However, PLA's inherent hydrophobicity and low osteoconductivity pose challenges for cellular adhesion and bone regeneration. To address these limitations, researchers have explored various strategies, including surface modifications and composite formulations. Incorporating materials such as collagen, gelatin, or bioactive molecules like RGD peptides into PLA scaffolds has been shown to improve cell attachment and osteogenic differentiation. Additionally, the base material can be combined with osteoinductive additives, such as hydroxyapatite and tricalcium phosphate ceramics, to enhance their mechanical strength and promote bone-like mineralization [4–6]Scaffolds, particularly those used in tissue engineering, are often designed to be white and translucent to balance mechanical integrity with biological functionality.

Additive manufacturing (AM), commonly known as 3D printing, has radically changed the creation of personalized scaffolds for bone tissue engineering by enabling precise customization of scaffold geometry, porosity, and mechanical properties to match individual patient anatomy. This customization is achieved by integrating patient-specific imaging data, such as CT or MRI scans, into the design process, enabling scaffolds that perfectly fit complex bone defects and promote optimal tissue integration. AM techniques, including extrusion-based methods like fused deposition modeling (FDM), were used in this study due to the fact that it offers advantages such as high resolution, design flexibility, and the ability to incorporate bioactive materials, enhancing scaffold functionality. These capabilities facilitate the development of scaffolds that not only support bone regeneration but also mimic the mechanical and biological properties of native bone, addressing the limitations of traditional implant materials and advancing personalized medicine in orthopedics [7–10].

Heterogeneous porosity is a critical design parameter in bone tissue engineering scaffolds, influencing biological performance and mechanical behavior. Microporosity enhances osteogenesis by increasing the scaffold's surface area, facilitating protein adsorption, and promoting cell attachment and infiltration. For bone tissue engineering, scaffolds range between 100 and 500 μm. Pores around 300–500 μm are optimal for promoting cell migration, vascularization, and nutrient diffusion, which are essential for bone regeneration. Smaller pores (50–100 μm) support early cell attachment and proliferation, while larger ones (200–400 μm) enable better tissue infiltration and blood vessel formation. The pore size should be tailored depending on the stage of healing and the specific application to achieve the best regenerative outcomes. It has been reported that pore sizes range from 200 to 1000 μm, and their shapes play a role in scaffolds as they serve as topological cues for cells, promoting cell adhesion and proliferation while influencing osteogenic differentiation [11–14].

From a mechanobiological perspective, scaffold porosity directly affects the mechanical stimuli experienced by cells, such as shear stress and strain, which are essential for mechanotransduction, the process by which cells convert mechanical stimuli into biochemical signals. Higher porosity typically results in lower wall shear stress (WSS) under fluid flow, which can influence cellular responses like

differentiation and matrix production. Furthermore, porosity impacts the scaffold's mechanical stiffness; lower porosity increases stiffness, leading to higher strain on attached cells, which can modulate gene expression related to osteogenesis. Therefore, optimizing porosity is essential to balance mechanical support with the biological cues necessary for effective bone regeneration [14–16]. PLA scaffolds, whether white or translucent, are highly influenced by printing parameters that dictate their mechanical properties and appearance. White PLA scaffolds are typically opaque due to the material's crystalline structure and are often used for applications requiring stronger mechanical properties, such as bone tissue engineering. The extrusion-based techniques, like Fused Deposition Modeling (FDM), are commonly employed, where printing parameters such as extrusion temperature, layer height, and print speed affect the porosity and rigidity of the scaffold. PLA scaffolds can be designed with varying pore sizes, and their mechanical strength is influenced by parameters like nozzle diameter and printing path density, making them suitable for load-bearing applications. These scaffolds can be further reinforced by incorporating bioactive fillers (e.g., hydroxyapatite), enhancing their mechanical properties while retaining opacity [13,17–22]. On the other hand, translucent PLA scaffolds are produced by adjusting the printing parameters to control the material's crystallinity. These scaffolds are generally more flexible and exhibit lower mechanical stiffness, making them suitable for softer tissue applications, such as cartilage. The translucency is achieved by optimizing print speed, layer thickness, and extrusion temperature, which affect the polymer's crystalline and amorphous regions [23–25].

Understanding the distinct characteristics of white and translucent PLA scaffolds is crucial for advancing their application in tissue engineering, as it enables a more precise selection of materials based on their biological, physical, and mechanical properties. By differentiating the effects of opacity and translucency on scaffold performance, we can better tailor scaffolds to specific tissue types and healing stages. This knowledge is pivotal in moving away from the indiscriminate use of PLA filaments and instead optimizing scaffold properties to meet the unique needs of each tissue engineering application. It also ensures that scaffolds are designed with appropriate biodegradability, porosity, and mechanical stability to support long-term tissue regeneration and integration, improving patient outcomes [26–31].

2. Materials and methods

2.1. Model architecture

2.1.1. Scaffold printing

The PLA scaffolds were fabricated using a Monoprice Select Mini 3D printer following the design reported by Pérez-Sánchez et al. The goal was to produce a scaffold with graduated porosity, three types of pores, a diameter of 9 mm, and a width of 1 mm. The scaffolds were printed using the parameters provided in the original design [11], with the settings applied using the Ultimaker Cura software to eliminate any variable changes. The major printing parameters were as follows: Temperature, 200 °C; printing speed, 10 mm/s; density fill, 20%; and layer height, 0.18 mm. These parameters were used to print 100 scaffolds, comparing translucent PLA filaments (commercially

available from 3D-Puebla) and white PLA filaments (from 3D-Market) (Figure 1), both with a diameter of 1.75 mm. The widths and diameters of the filaments were measured to ensure consistency [11].

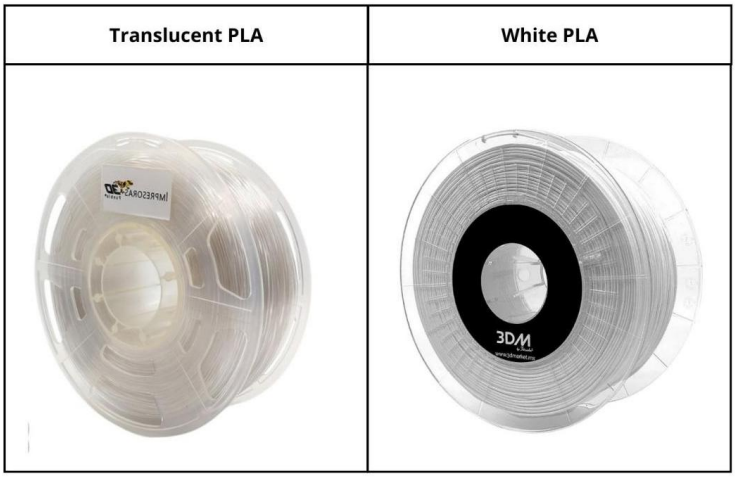

Figure 1. PLA filaments. Translucent and white PLA filament used to print the 3D scaffolds.

2.1.2. Scaffold printing superficial structure evaluation and energy Dispersive X-ray Spectroscopy (EDS)

The structure of the 3D-printed scaffolds was examined using scanning electron microscopy (SEM, JEOL 5600 LV) at 25 kV. The samples were sputter-coated with a thin gold layer to facilitate surface structure analysis. Elemental analysis of the scaffolds was carried out using Energy Dispersive X-ray Spectroscopy (EDS). The measurements were performed using a JEOL JSM-7800 Schottky Field Emission Scanning Electron Microscope. Both equipment pieces are at the Laboratorio Central de Microscopia, Institute of Physics, UNAM.

2.1.3. Porosity percentage

Six white and translucent scaffolds were individually weighed. Milli-Q water (100 mL) was then measured and retained in a beaker, and then weighed on a scale. Three weight measurements were performed: (Wdry) the weight of the dry scaffold, (Wsat) the weight of the scaffold when submerged in water, and (Wsus) the weight of the scaffold after being submerged for 30 min. Each weight was recorded, and the porosity percentage was calculated using the following formula.

$$\left(\frac{\boldsymbol{Wsat - Wsus}}{\boldsymbol{Wsat - Wdry}}\right)\mathbf{100}\% \quad [27]$$

Where:

$Wsat$=Saturated weight

W_{dry}=Dried scaffold weight

W_{sus}=Suspended scaffold weight

W=Weight

2.1.4. Diffuse reflectance measurements (optical absorption)

Optical absorption measurements were conducted at the Laboratorio Universitario de Óptica de Superficies, Physics Institute, UNAM. Three samples of each scaffold were used for measurements. A commercial reference from Ocean Insight enabled absolute measurements using a USB2000+ spectrometer from the same company. A commercial probe for diffuse reflectance measurements (QR400-angle-UV) was used. Special care was taken to ensure a consistent measurement procedure for all samples. Diffuse reflectance quantifies the scattering and optical absorption from non-specular surfaces, making it an ideal method for characterizing the optical response of heterogeneous scaffold surfaces. To calculate the absorbance from the reflectance data, the measurements were processed using the Kubelka-Munk formalism [32].

2.1.5. Fourier transform infrared (FTIR) spectrometry

FTIR analysis was conducted to identify the functional groups and possible differences between the translucent and white composite scaffolds. The experiment was carried out using a VERTEX 70v Bruker Fourier Transform Infrared (FTIR) spectrometer, in the wavelength range of 4000–500 cm^{-1}.

2.1.6. Raman spectroscopy

Raman scattering measurements were performed using a Horiba Xplora Plus Raman spectrometer. Spectra were recorded using an excitation wavelength of 532 nm and collected with a 10× objective lens. Each measurement was acquired with an integration time of 1 second and 100 accumulations. The Raman shift range was set between 100 and 3500 cm^{-1}. The Raman signal was dispersed using a diffraction grating with 1200 grooves/mm.

2.2. In vitro and in vivo response

2.2.1. Cell culture

The Fetal Human Osteoblast cell line (hFOB 1.19 ATCC® CRL-11372) was cultured in Dulbecco's Modified Eagle Medium: Nutrient Mixture F12 (DMEM : F12, GIBCO) supplemented with 10% fetal bovine serum (FBS, GIBCO) and an antibiotic solution (penicillin 1000 IU/mL, streptomycin 100 µg/mL, and fungizone 0.3 µg/mL). The culture was maintained at 37 °C in 95% air atmosphere with 5% CO_2 and 100% humidity. The scaffolds were sterilized with ethylene oxide gas prior to biological assays. On the third day of culture, the medium was replaced with an osteogenic differentiation induction medium containing 50 µM ascorbic acid, 10 mM β-glycerophosphate,

and 10^7 M dexamethasone. The volume of medium per scaffold corresponds to 300 μL. We used Corning 48-well cell culture plates for seeding and incubation period, and Corning 96-well cell culture plates for absorbance reading.

2.2.2. Cell viability assay (WST-1)

The viability of hFOB cells seeded at 2×10^4 cells/mL onto the 3D-printed scaffolds was evaluated using the WST-1 assay at 3, 7, and 14 days of culture. Cells on the culture plate were positive controls. The assay was performed according to the manufacturer's instructions for the Cell Proliferation Reagent WST-1 (Sigma-Aldrich). This assay relies on the ability of the mitochondrial dehydrogenase enzyme to reduce the WST-1 insoluble salt to a water-soluble formazan dye. When cells are metabolically active, enzyme activity increases the production of formazan, which correlates directly with the number of viable cells. At the specified time points, the cultures were incubated with 20 μL of WST-1 reagent suspended in 200 μL of culture medium for 4 h, after 100 μL of the solution was removed to measure the absorbance at 450 nm using a plate reader (ChroMate, Awareness Technology). The percentage of viable cells was calculated using the following formula:

$$\boldsymbol{Viability}\ \% = \left(\frac{\boldsymbol{Experimental\ OD\ 450}}{\boldsymbol{Control\ OD\ 450}}\right)\boldsymbol{100} \quad [29]$$

Alkaline phosphatase (ALP): Osteogenic differentiation of hFOB cells on the 3D-printed scaffolds was assessed by measuring alkaline phosphatase (ALP) activity at 3, 7, and 14 days of culture. ALP activity was measured using the manufacturer's colorimetric assay kit (Abcam, Cambridge, United Kingdom). After the culture period, the cell layers were lysed using lysis buffer (Gibco), and 80 μL of the lysate was incubated with 50 μL of 5 mM pNPP solution at 25 °C for 1 h. After incubation, ALP activity was measured at 405 nm and the enzyme activity was quantified using a standard curve. Cells on the culture plate were positive controls.

2.2.3. Alizarin red assay

Alizarin Red Staining (ARS) was used to detect calcium deposits formed during osteogenic differentiation of hFOB cells cultured on the 3D-printed scaffolds after 7 and 14 days. ARS (Sigma-Aldrich) was used for this procedure. The scaffolds were carefully washed with PBS and fixed in 4% paraformaldehyde for 24 h, followed by three washes with distilled water. The scaffolds were then stained with a 40 mM ARS solution at pH 4.2 for 30 min. After incubation, the ARS solution was removed and the scaffolds were washed with distilled water. Excess dye was removed, and images were captured using a stereoscopic microscope (Olympus DSX-HRSU, Tokyo, Japan).

2.2.4. Cell morphology onto 3D-printed scaffolds

SEM was used to evaluate cell morphology and extracellular matrix formation in the white and translucent 3D-printed scaffolds after 14 days of culture. The samples were sputter-coated with a thin gold layer to facilitate the observation of cell-material interactions.

2.2.5. Surgical procedure

The procedure adhered to the guidelines set forth by the Official Mexican Norm NOM-062-ZOO1999, ARRIVE guidelines 2.0, and was approved by the Institutional Animal Care and Use Committee (IACUC) under authorization number FO-M001-0009-2021.

Three experimental groups of four rats were each randomly assigned to the evaluation periods of 7, 21, and 41 days; a control group was not used because it does not provide essential information to answer the hypothesis, and this minimizes the use of animals. Twelve male Wistar rats weighing 250 g (from Unidad de Modelos Biologicos, Biomedical Research Institute, UNAM) were used to assess the inflammatory response to each scaffold (white and translucent) in subcutaneous tissue. Cochran's formula was used to calculate the sample size ($n = Z^2 \cdot p \cdot (1-p)/d^2$), obtaining N = 12 animals (3 groups of 4), where 95% confidence level is Z = 1.96, expected proportion of success or prevalence p = 0.5, accepted margin of error d = 28.3% which ensures a sufficient size to evaluate qualitative histological findings and guarantee adequate representativeness of the experimental model [33].

Inclusion criteria. Male rats, weighing 250 g, normal response to environmental stimuli, as assessed by the Grimace Scale [34], indicating the absence of signs of distress or discomfort, the animals were clinically healthy, with no signs of disease, including the absence of weight loss and normal fecal consistency. Exclusion criteria

Female rats, weighing over or under 250 g, abnormal response to environmental stimuli, as assessed by Grimace Scale, clinically unhealthy animals (weight loss, diarrhea or bloody feces, and changes in food and water consumption). However, no animal was excluded from the experiment. As the scaffolds were implanted in the exact anatomical location for all animals, the researchers were not blinded. However, the expert pathologist responsible for histological analysis remained unaware of the group assignments. Each rat was weighed and marked for identification with numbers, assigning two rats per cage. The rats were then gently anesthetized with ketamine (80 mg/kg) and isoflurane (SOFLORAN VET) using a Somnosuite anesthesia system (Kent Scientific corporation). After sedation, the backs of the rats were shaved carefully.

Antiseptic and aseptic procedures were performed on the back, with povidone iodine (Yodo desinfectante, ARANDA). A 2 cm incision was made, and the tissue was separated using a Halstead clamp to create a flap-like envelope. The scaffolds were implanted on each side of the backs of the rats, positioned as far from the incision as possible, with the white scaffold on the left side and translucent scaffold on the right side. The incisions were then sutured using 3-0 polyglycolic acid (Figure 2). Postoperative clinical follow-up was subsequently performed, assessing a series of parameters: Animal's general condition, pain scale (Rat Grimace Scale), wound appearance, bleeding, exudate, or collections or extrusion of biomaterials. The rats were kept under 12-hour photoperiod conditions and 50% relative humidity and were fed Rodent Diet 5001 ad libitum.

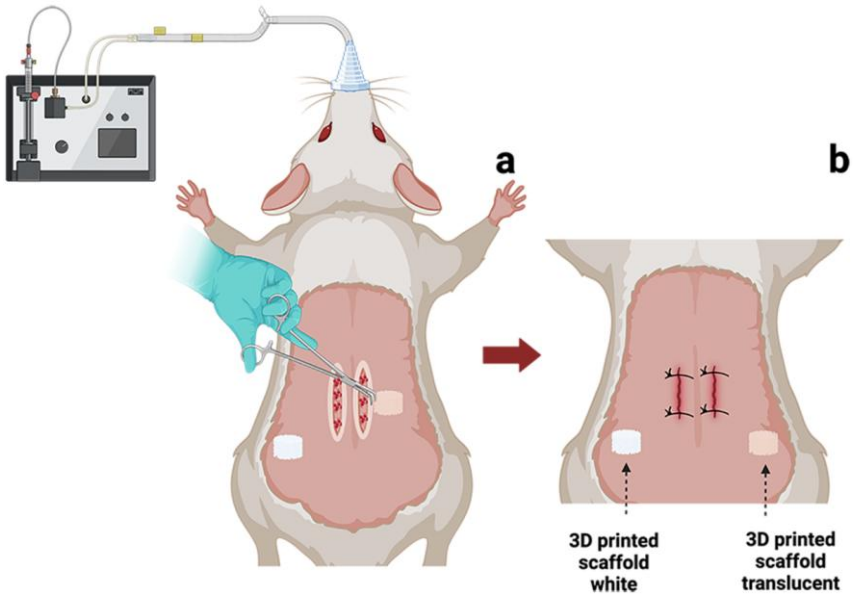

Figure 2. Schematic of the surgical procedure. (a) An envelope-shaped flap is created on the torso of a sedated and tranquilized rat, and the scaffold is implanted into the subcutaneous tissue of the back, positioned as far from the incision as possible. (b) The incision is sutured with 3-0 polyglycolic acid, and post-surgical follow-up is conducted to monitor the animal's general condition and assess the inflammatory response at 7, 21, and 41 days.

2.2.6. Animal euthanasia

Once the evaluation periods (7, 21, and 41 days) were concluded, animal euthanasia was performed following the protocol outlined in the Norma Oficial Mexicana NOM-062-ZOO1999. Carbon monoxide was used to induce painless and humane death by causing cardiorespiratory failure.

2.2.7. Histology slide

The samples were collected at 7, 21, and 41 days, ensuring a 1 mm safety margin around the scaffold. The samples were fixed in 10% formalin for 24 h for histological analysis. Serial sections, 5 µm thick, were prepared and stained with hematoxylin and eosin for observation under an optical microscope.

2.2.8. Statistical analysis

The WST-1 and alkaline phosphatase results were analyzed using two-way ANOVA with a post-hoc Tukey test. The Student's t-test was performed to determine the porosity percentage. Results were considered statistically significant at p-values < 0.05 (*), < 0.01 (**), and < 0.001 (***).

3. Results

3.1. Material and surface

3.1.1. Scaffold printing

Nine printed scaffolds were tested under each condition. The 3D-printed scaffold using white filament had a diameter of 9.15 mm ± 0.56 mm and a width of 1.01 mm ± 0.2 mm, while the scaffold printed with translucent filament measured 8.96 mm ± 0.85 mm in diameter and 0.97 mm ± 0.3 mm in width (Figure 3). Additionally, the surface structure, evaluated using stereoscopic microscopy, revealed that the pore and microchannel formation in the 3D-printed scaffold with white filament maintained a better structural definition than the scaffold printed with translucent filament, where the pores and microchannels were clogged.

3.1.2. Superficial structure evaluation

Figure 3 shows the SEM images of the surface structure of the 3D-printed scaffolds. SEM analysis revealed that the scaffold printed with PLA filaments exhibited a poorly defined layer-by-layer structure with pores obstructed by the printing material. At the center of the microchannels, a thicker fiber was visible along with areas of melted material near the edges of the microchannels. In contrast, the scaffold printed with white PLA filaments displayed clear layer-by-layer delineation with well-defined edges and varying pore sizes. A thin fiber was observed between the microchannels; however, these fibers did not obstruct the microchannels.

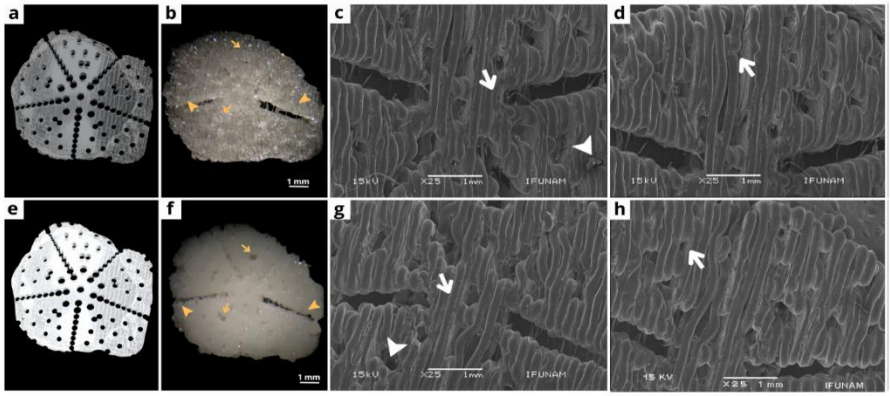

Figure 3. Surface structure of 3D-printed scaffold. (a) Original scaffold design. (b) The translucent PLA 3D-printed scaffold, with arrowheads indicating the obstructed entrances of the microchannels, and the arrow pointing to the obstructed pores. (c) The arrow points to a fiber collapsing a pore, in contrast to the image. (d) The arrow highlights layer discontinuity in comparison to the image. (e) Original scaffold design. (f) White PLA 3D-printed scaffold, with arrowheads showing that the microchannels have a homogeneous structure, unobstructed by material; arrows indicate the original morphology of the pores. (g) The arrow points to uniform layers, with the arrowhead displaying a well-defined pore. (h) Microchannels with fine fibers in between.

3.1.3. Energy dispersive X-ray spectroscopy (EDS) analysis

Elemental analysis of the translucent and white scaffolds revealed no differences in terms of the major elements present in the PLA filament, which are carbon and oxygen, indicating a high degree of material purity (Figure 4). However, the analysis did not detect any additional elements that would suggest the inclusion of additives, such as whitening agents.

The translucent scaffold exhibited an average carbon content of 61.37 ± 3.96 wt% and 38.64 ± 3.95 wt% oxygen (Figure 4a,b). In comparison, the white scaffold showed an average of 56.28 ± 1.82 wt% carbon and 43.66 ± 1.92 wt% oxygen (Figure 4c,d).

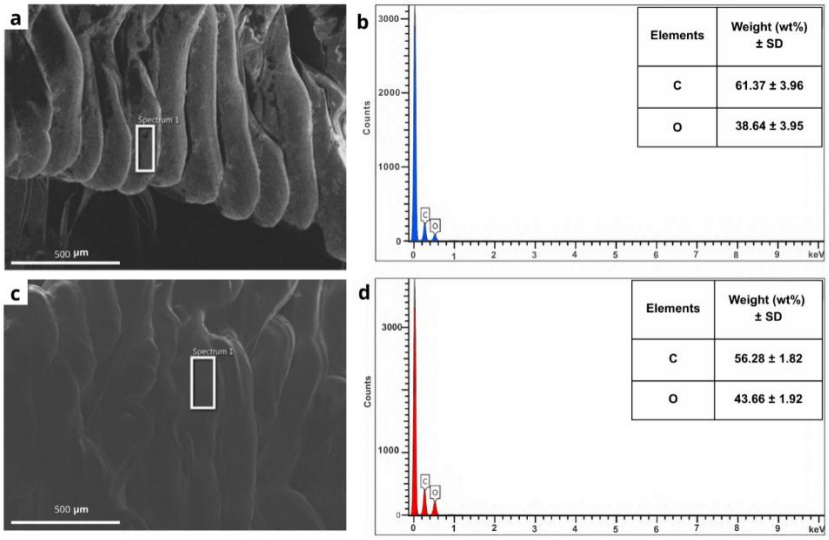

Figure 4. SEM micrographs and EDS analyses of PLA scaffolds. (a) SEM image of the translucent scaffold. (b) EDS spectrum of the translucent scaffold, including a table showing the weight percentage (wt%) of carbon and oxygen. (c) SEM image of the white scaffold. (d) EDS spectrum of the white scaffold, with a table indicating the weight percentage (wt%) of each element. In both cases, the elemental analysis confirms that carbon and oxygen are the major constituents, consistent with the chemical composition of PLA.

3.1.4. Pore size and porosity

Analysis of the pore size distribution diameter using ImageJ software showed that the 3D-printed scaffolds made with translucent PLA filaments had a pore size distribution ranging from 100 to 700 µm, with an average pore size of 363 ± 129 µm (Figure 5a). In contrast, the pore sizes of the 3D-printed scaffolds made with white PLA filaments ranged from 200 to 800 µm, with an average size of 314 ± 119 µm (Figure 5).

The porosity of the scaffolds was evaluated as a general property and compared between translucent and white 3D-printed scaffolds. Figure 5 shows the porosity percentage of each scaffold calculated using Archimedes' principle. The translucent PLA scaffolds exhibited a porosity of 53%, whereas the white PLA scaffolds had a porosity of 67%. Student's t-test was performed with a p-value < 0.05, showing no statistically significant difference between the two groups.

3.1.5. Diffuse reflectance measurements (optical absorption)

The absorbance of the translucent scaffolds exhibited an inhomogeneous optical response across the samples studied, as shown in Figure 5c. This inhomogeneity can be attributed to the less-defined structure of the translucent scaffolds. In contrast, the more defined structure of the white scaffolds, despite their larger porosity, resulted in more homogeneous absorbance. In other words, the more structured pores in the white scaffolds allowed for more uniform absorbance measurements, whereas the loss of structure in the pores of the translucent scaffolds led to more scattered reflectance. This finding highlights the importance of maintaining pore definition for a better cellular response, a topic that will be discussed in detail below. Conversely, although the white scaffolds were more porous, they exhibited a more homogeneous absorbance, as shown in Figure 5d, for the different samples studied, with a well-defined absorption band between 425 nm and 560 nm.

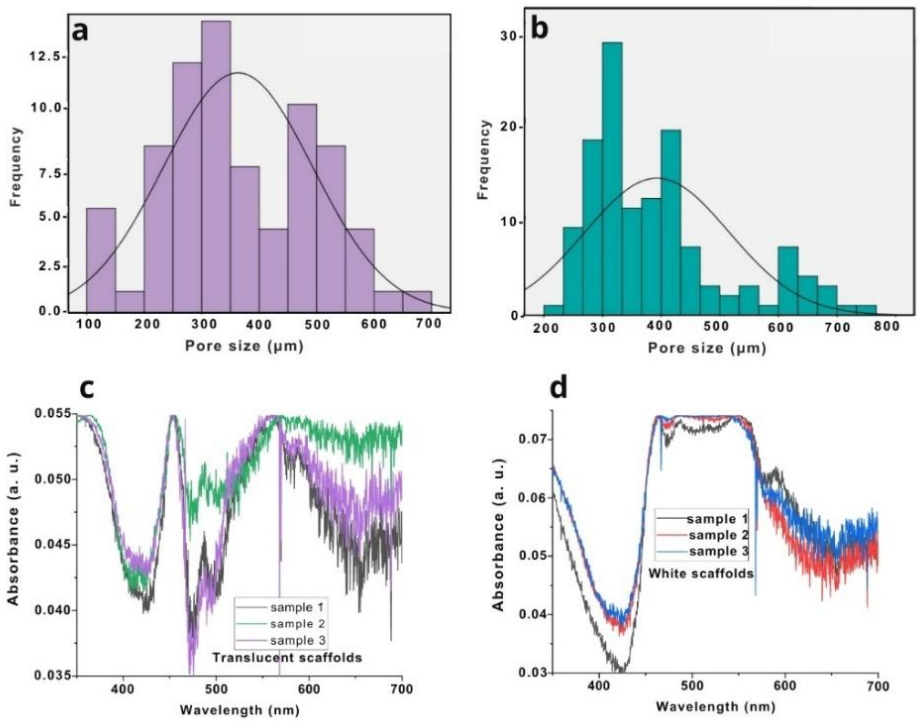

Figure 5. Optical absorption and pore size. (a) Histogram showing the distribution of pore sizes in the white 3D-printed scaffolds. (b) Histogram showing the distribution of pore sizes in the translucent 3D-printed scaffolds. (c) Optical absorption of the white scaffold. (d) Optical absorption of the translucent scaffold.

3.1.6. FTIR analysis

FTIR spectroscopy was conducted to identify potential additives or pigments in the white PLA-printed scaffold, compared to the translucent PLA scaffold. Both samples exhibited characteristic absorption bands corresponding to pure PLA. The band at 1081 cm^{-1} is attributed to C–O stretching

vibrations, while the peak at 1452 cm^{-1} corresponds to CH_3 bending. A strong absorption at 1746 cm^{-1} is assigned to C=O stretching, and the band at 2932 cm^{-1} also represents CH_3 bending vibrations. These findings confirm the presence of typical functional groups associated with pure PLA in both scaffolds. However, an additional absorption band was detected in the white PLA scaffold within the range of 1000 to 900 cm^{-1}, which was not present in the translucent PLA. In Figure 6 (a), this unique peak is highlighted within a black box for visual reference.

3.1.7. Raman spectroscopy analysis

Raman spectroscopy was performed to further investigate the molecular structure of the white and translucent PLA scaffolds and to identify any spectral differences between them. Both samples exhibited characteristic Raman bands of polylactic acid (PLA). A peak at 874 cm^{-1} was assigned to C–COO stretching, associated with ester groups in the polymer structure. The bands at 1127 cm^{-1} and 1454 cm^{-1} were attributed to CH_3 symmetric and asymmetric bending vibrations, respectively. A strong band at 1774 cm^{-1} was assigned to C=O stretching, and the peak at 2948 cm^{-1} corresponded to CH_3 stretching vibrations. These signals confirm the presence of functional groups typically associated with PLA in both scaffold types. A notable difference was observed in the white PLA scaffold, which exhibited an additional Raman band in the 2500–2800 cm^{-1} range. This signal was absent in the translucent PLA scaffold. As shown in Figure 6 (b), this additional band is highlighted with a black box for visual reference.

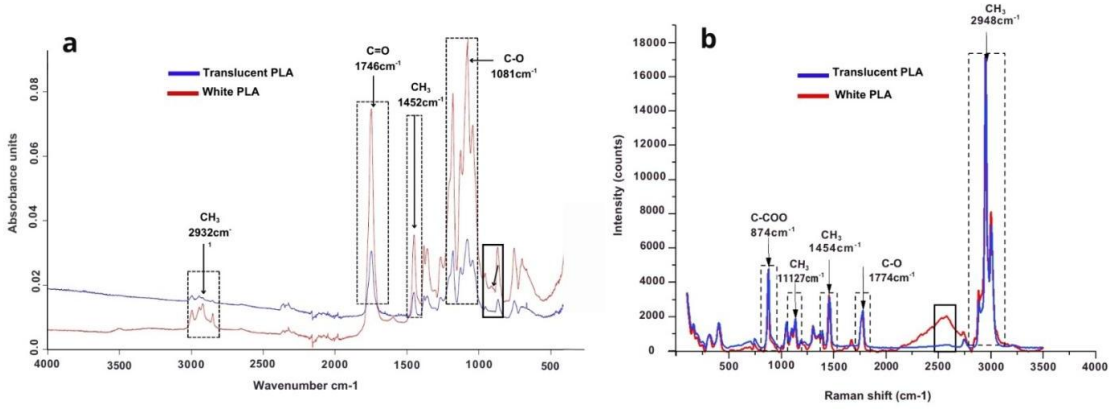

Figure 6. FTIR and Raman spectra of translucent and white PLA scaffolds. **(a)** FTIR spectra of both scaffolds showing characteristic absorption bands of PLA, including C–O stretching (1081 cm^{-1}), CH_3 bending (1452 cm^{-1}), C=O stretching (1746 cm^{-1}), and CH_3 bending (2932 cm^{-1}). An additional band observed only in the white PLA scaffold between 1000 and 900 cm^{-1} is highlighted in a black box. **(b)** Raman spectra of both scaffolds, showing typical PLA bands: C–COO stretching (874 cm^{-1}), CH_3 bending (1127 and 1454 cm^{-1}), C=O stretching (1774 cm^{-1}), and CH_3 stretching (2948 cm^{-1}). A distinct Raman band, present only in the white PLA scaffold in the 2500–2800 cm^{-1} region, is also highlighted with a black box.

3.2. In vitro and in vivo response

3.2.1. Cell viability assay (WST-1)

Cell viability measured by the WST-1 assay using human fetal osteoblastic cells (hFOB) showed significant differences between the white and translucent 3D-printed scaffolds after three days of the study, with viability percentages of 70% and 39%, respectively. The white 3D-printed scaffolds exhibited a better response. However, at 7 and 14 days, no significant differences were observed (Figure 7a).

3.2.2. Alkaline phosphatase (ALP)

ALP assay was conducted to evaluate the osteogenic activity of osteoblasts on the 3D-printed translucent and white scaffolds after 3, 7, and 14 days. Figure 7b shows that after three days, the translucent 3D scaffolds exhibited higher ALP activity than the white 3D scaffolds. After 7 days, there was an increase in ALP activity in the white 3D-printed scaffolds compared to that in the translucent 3D scaffolds. At 14 days, a decrease in ALP activity was observed in the white scaffolds relative to that in the translucent scaffolds, with no statistically significant difference between the groups.

3.2.3. Alizarin red assay

The Alizarin Red Staining (ARS) assay was used to visually detect calcium deposits formed by hFOB cells on 3D-printed translucent and white scaffolds after 7 and 14 days. Figure 7c–h shows ARS staining after 7 and 14 days. The red coloration is more pronounced on the surface of the 3D white-printed scaffold compared to the lighter red staining observed on the surface of the 3D translucent-printed scaffold. However, in both scaffolds, ARS staining was visible, indicating calcium deposition by osteoblast cells on the surface.

3.2.4. SEM superficial structure on 3D scaffolds with cells

The interaction of the osteoblast cells with the surface of the 3D white and translucent printed scaffolds was analyzed using SEM after 14 days of culture. Figure 7i–l shows a similar interaction and matrix deposition behavior by osteoblasts on the surface of both the 3D-printed scaffolds. Furthermore, in the white 3D scaffold, matrix deposition appeared as a more homogeneous layer compared to the translucent scaffold, where some spaces were visible.

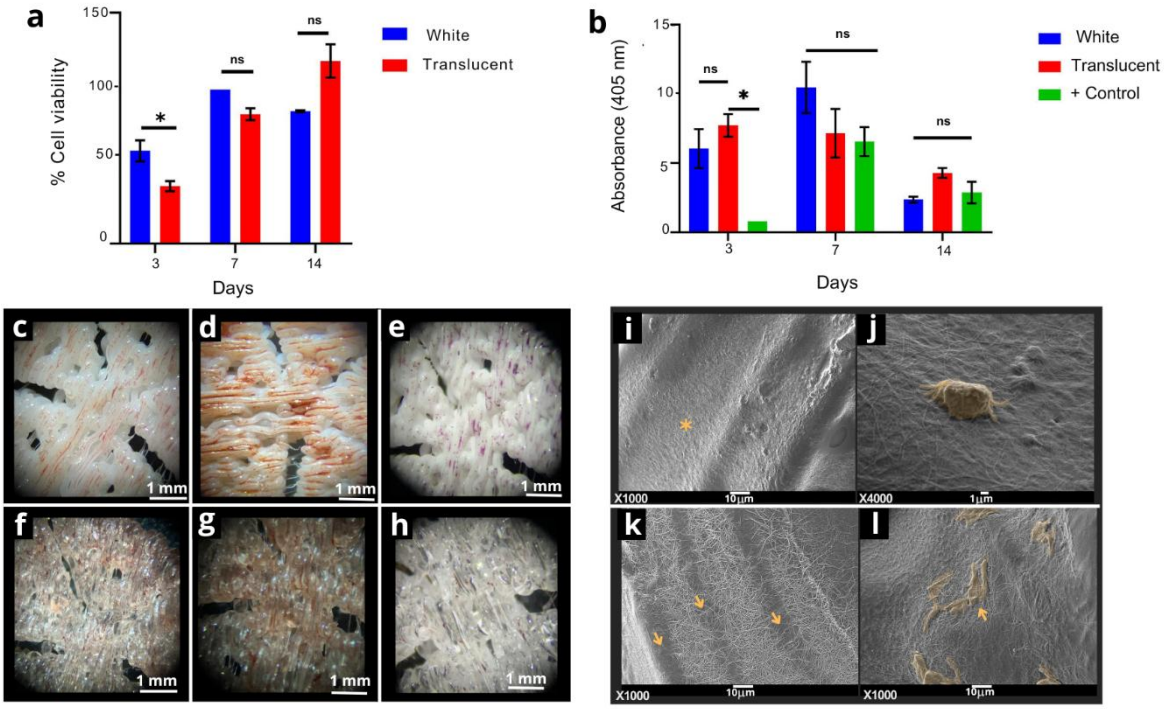

Figure 7. In vitro assays and SEM images. (a) Cell viability assay comparing white versus translucent 3D-printed scaffolds. Asterisks indicate a statistically significant difference (*p < 0.05), and ns indicates no significant difference. (b) Alkaline phosphatase assay of translucent versus white 3D-printed scaffolds, with asterisks denoting significant differences (*p<0.05). Alizarin Red staining after 7 days: (c) White and (f) translucent; and after 14 days: (d) White and (g) translucent. The positive control is shown in (e) for white and (h) for translucent scaffolds. Surface morphology of the 3D-printed scaffolds after 14 days of culture with hFOB: (i) A homogeneous matrix covers the surface of the 3D white-printed scaffold. (j) Higher magnification of the surface of the 3D white-printed scaffold showing matrix deposition with cellular conglomerates (yellow). (k) Matrix deposition observed on the 3D translucent printed scaffold, with visible spaces in between (arrows). (l) Higher magnification of the 3D translucent printed scaffold surface, showing cellular groupings with apparent communication (yellow); the arrow indicates these are covered by a matrix.

3.2.5. Histological response

We evaluated the histological response at 7, 21, and 41 days after implantation of white and translucent scaffolds into the subcutaneous tissue on the backs of Wistar rats. The samples were sectioned to 5 µm thickness, stained with hematoxylin and eosin, and examined under a light microscope at 10x magnification.

After 7 days, the white scaffold exhibited an acute inflammatory response, with moderate inflammatory cells and blood vessel formation. A fibrous capsule was observed surrounding the lumen where the scaffold was placed (Figure 8a). In contrast, the translucent scaffold showed a more intense

acute inflammatory response, with fewer blood vessels. Figure 8d illustrates a thicker fibrous capsule surrounding the lumen than the white scaffold.

By day 21, the white scaffold implantation area revealed dense fibrous tissue with numerous foreign-body-type giant cells. The lumen displayed poor blood vessel formation and a thicker fibrous connective tissue capsule (Figure 8b). The response to the translucent scaffold was characterized by a chronic inflammatory infiltrate with fewer foreign body-type giant cells and minimal blood vessel formation. The capsule primarily comprised fibrous connective tissue, with no tissue extending towards the lumen (Figure 8e).

At 41 days, the response to the white scaffold showed minimal chronic inflammatory infiltration, no foreign body-type giant cells, moderate blood vessel formation, and a developed fibrous connective tissue capsule (Figure 8c). The translucent scaffold response included a small number of chronic inflammatory cells, mild blood vessel formation, and loose fibrous connective tissue (Figure 8f).

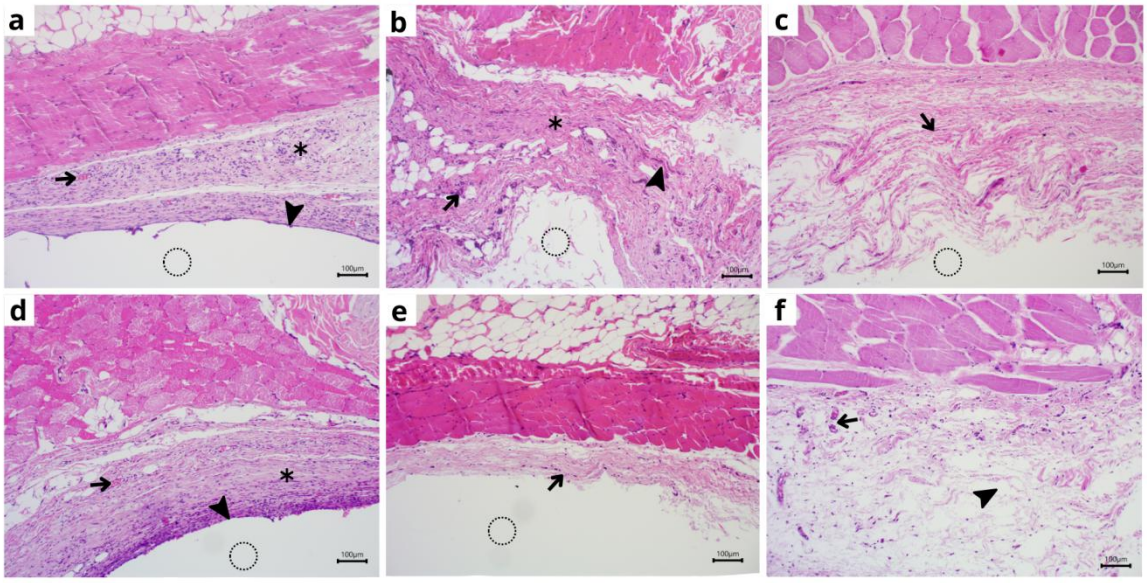

Figure 8. *In vivo* histology. (a) The white scaffold exhibits a mild acute inflammatory response (asterisk). The dotted circle indicates the implant. (d) The translucent scaffold displays a stronger acute inflammatory response (asterisk). The dotted circle represents the implant. In both images, the arrow points to blood vessels, while the arrowhead indicates the formation of a fibrous capsule. (b) The white scaffold shows numerous foreign body-type giant cells (arrows), with moderate blood vessel formation indicated by the arrowhead and dense fibrous connective tissue marked by an asterisk. The dotted circle represents the implant. (e) The translucent scaffold presents dense fibrous connective tissue (arrow). The dotted circle indicates the implant. Histological images at 41 days of evaluation. (c) The arrow in the white scaffold image points to the fibrous connective tissue capsule. The dotted circle indicates the implant. (f) The arrow in the translucent scaffold image shows loose, disorganized fibrous connective tissue.

4. Discussion

PLA is a widely used polymer in bone applications, as demonstrated in several 3D-printed scaffold studies [30,31,35,36]. In tissue engineering, commonly used filaments are typically translucent or white-pigmented. However, the literature reviewed in this article primarily focuses on the impact of PLA color in FDM-printed parts, examining factors such as surface quality, layer deposition variation, dimensional accuracy, thermal behavior, and filament surface characteristics (e.g., the presence of bubbles and surface tension). These factors are critical because they directly influence the properties of the printing material, which in turn affect the mechanical properties of the scaffolds and the need for standardization [19–22].

Therefore, the selection of materials and their surface characteristics, including those related to PLA color, are crucial for the design of scaffolds for tissue engineering applications. However, the literature remains limited regarding the influence of color variations on the physicomechanical properties and biological responses of these scaffolds. We aimed to provide empirical evidence on how different PLA colors affect in vitro and in vivo outcomes, offering valuable insights for optimizing the design and application of these materials in medical applications.

Surface evaluation of the scaffolds was performed using stereomicroscope images (Figure 2), where both scaffolds exhibited differences in their surface characteristics, with the white scaffold showing better pore definition. SEM images revealed that the 3D-printed white PLA scaffold maintained its fidelity of detail, with well-defined microchannels and pores. In contrast, the translucent PLA scaffold displayed undefined pores and microchannels obstructed by the material (Figure 3).

Valerga et al. reported that translucent PLA filaments exhibit higher wettability, the ability of the polymer to spread over a solid surface, compared to pigmented filaments, which was attributed to their lower surface tension. This property directly influences the material's behavior during the extrusion process, enhancing its flowability and spreading capacity [20].

On the other hand, Frunzaverde et al. compared black-pigmented PLA with natural PLA and found that the former exhibited better dimensional accuracy, attributed to a higher degree of crystallinity [21]. Increased crystallinity in PLA has been shown to correlate with a higher elastic modulus and tensile strength, making pigmented PLA scaffolds (e.g., white) more suitable for mimicking dense and mineralized biological environments such as bone tissue.

In contrast, other authors have reported that translucent PLA generally exhibits lower crystallinity, which results in greater flexibility and reduced mechanical stiffness. These properties make translucent PLA more appropriate for soft tissue applications, such as cartilage, where structural adaptability is essential [19,22,37]. Additionally, this lower crystallinity promotes higher melt flow during extrusion, enabling better pore filling and reproduction of fine details, though at the expense of precision in micrometric features.

Conversely, white pigmented PLA, due to the inclusion of pigments and additives, tends to display higher viscosity, allowing for improved control over material deposition and greater fidelity in detail reproduction [19]. These factors may help explain the partial pore obstruction observed in the translucent scaffolds in this study, despite identical printing parameters being used for both scaffold types.

This highlights the importance of selecting the appropriate PLA filament based on the specific requirements of the target tissue, rather than using PLA filaments interchangeably in tissue engineering. Such selection is crucial to optimize both the mechanical performance and the biological response of the printed scaffolds [38].

Furthermore, although several authors have identified printing temperature as a critical factor affecting the quality and resolution of 3D-printed constructs [39–41], both scaffolds in this study were printed using the same temperature settings, as recommended by the manufacturer for the PLA filament. As Valerga et al. emphasized, it is essential that manufacturers regulate these parameters. Otherwise, modifying the printing temperature without knowing the precise pigment composition, which is typically undisclosed, would be arbitrary and technically unfounded [37].

To identify the pigment component in the white PLA scaffold, EDS, FTIR, and Raman spectroscopy analyses were performed. EDS analysis revealed only carbon and oxygen in both scaffolds. However, FTIR analysis of the white PLA scaffold showed an additional absorption band between 1000 and 900 cm^{-1}, absent in the translucent PLA. This suggests the presence of a pigment or additive.

Titanium dioxide (TiO_2) is commonly used as a white pigment in polymers, including PLA. However, pure TiO_2 typically shows characteristic peaks below 800 cm^{-1}[42], which does not match the observed FTIR signal. Literature reports that TiO_2 can be functionalized with silica (SiO_2) to improve its adhesion and dispersion in polymer matrices [43]. This functionalization introduces siloxane (Si–O) bonds that exhibit IR absorption bands in the 1000–900 cm^{-1} range, which could explain the additional signal observed in our FTIR analysis.

Additionally, Raman spectroscopy of the white PLA scaffold revealed a distinct band in the 2500 cm^{-1} region, which was not observed in the translucent PLA. This signal does not correspond to TiO_2 or its silica-functionalized form, suggesting the possible presence of another additive, impurity, or contaminant yet to be identified.

To confirm the presence and identity of the pigment or additive in the white PLA scaffold further, more sensitive analytical techniques are recommended. In particular, X-ray fluorescence spectroscopy (XRF) and X-ray photoelectron spectroscopy (XPS) could be useful for detecting trace elements such as titanium (Ti), silicon (Si), or sulfur (S), which may be below the detection limit of EDS analysis.

Regarding the importance of maintaining pore definition and size in scaffolds, researchers have suggested that pore sizes favorable for bone regeneration range from 100 to 1000 μm. Although no ideal pore size has been universally established, sizes between 100 and 400 μm have been reported to enhance cell adhesion and proliferation, and even influence osteogenic differentiation. Pores ranging from 500 to 1000 μm favor vascularization [9,44–46]. In this study, when measuring the pore sizes of the white and translucent scaffolds, we found that the pores in the center of the scaffold ranged from 500 to 700 μm in diameter, decreasing towards the edge to a range of 200–400 μm (Figure 5). These findings consider both the cellular responses and vascular ingrowth. However, differences were observed when the percentage of porosity of the scaffolds was measured. This difference corresponds to what was observed in the microphotographs and the pore obstruction present in the translucent scaffold. Porosity affects nutrient permeability and oxygen exchange, which are crucial for regenerative processes. This suggests that the porosity percentages of both scaffolds are beneficial for regeneration [1]. These structural conditions are supported by the optical responses of the scaffolds.

The more homogeneous absorbance of the white scaffold, despite its larger porosity, can be related to the better definition of the pores and pore sizes compared with the translucent scaffold. Studies have revealed the role of specific biomaterials and structural designs in enhancing the osteogenic performance of PLA scaffolds. A study by Zhao et al. introduced a periosteum-bone-inspired bilayer scaffold incorporating piezoelectric properties, which significantly improved osteogenesis, angiogenesis, and neurogenesis, thereby promoting neuro-vascularized bone regeneration. Similarly, research by Li et al. demonstrated that incorporating immunomodulatory RNA-based biomaterials into collagen scaffolds effectively modulated the local immune environment, facilitating bone regeneration through macrophage polarization via the JAK2/STAT3 signaling pathway. Additionally, a study by Zhang et al. highlighted that integrating PHA and PBT into piezoelectric periosteum biomaterials enhanced their physicochemical properties and biological functions, leading to improved surface hydrophilicity, mechanical performance, and endogenous electrical stimulation, all contributing to accelerated bone regeneration. These findings underscore the importance of biomaterial composition and structural design in modulating the biological mechanisms underlying bone regeneration, offering valuable insights for optimizing PLA-based scaffolds in tissue engineering applications [47–49].

Regarding the in vitro cellular results, viability assays (WST-1), alkaline phosphatase assays (ALP), and Alizarin Red assays (ARS) were performed to determine whether the change in pigment in the 3D-printed scaffolds influenced cellular response. The viability results showed a significant difference on day 3, favoring the white scaffold over the translucent one, with increased activity levels on day 7 in both groups, although no statistical difference was observed. These results are consistent with those of other authors who printed PLA scaffolds without considering the pigmentation of the material, such as Pant et al. [31]. In their study, cell viability assays showed an increase from day 7, demonstrating that human osteosarcoma cells in PLA-printed scaffolds became more active as the days progressed, without any surface modification [50–52]. Similarly, Wo et al. reported in their study that Ti-6Al-4V scaffolds with a high percentage of porosity and larger pore sizes favored osteoblast viability, whereas those with less porosity resulted in lower cell viability [53]. These findings are consistent with the results of this study. On day 3 of the cell viability assay, the translucent scaffold showed lower porosity and cell viability than the white scaffold, which had better pore definition and porosity. This emphasizes the importance of optimizing the scaffold design with appropriate pore sizes, as researchers have established that porosity not only facilitates the exchange of oxygen and nutrients between cells, but is also directly related to protein absorption and cell adhesion, critical processes that influence early cell viability. Nevertheless, the cell viability assays showed a decrease on the 7th and 14th day, which can be related to the cell's capacity to secrete extracellular matrix, bearing in mind that DMEM F-12 medium is supplemented with osteogenic inducers such as ascorbic acid, dexamethasone, and β-glycerophosphate.

Conversely, ALP levels peaked on day 7 and decreased by day 14, with no statistically significant differences between the two groups. These results align with the literature, which suggests that ALP activity is an early marker of osteoblastic differentiation and is necessary for hydroxyapatite formation [1]. Regarding the ARS assay, calcium nodules were observed on the scaffold surface, concentrating around the pores and between the filament layers in both groups. The white PLA scaffold exhibited more red staining than the translucent scaffold after both 7 and 14 days, which was consistent with the function of ARS in detecting calcium deposits, indicating osteoblast maturation and

mineralization. Moreover, the control group (white and translucent scaffolds without cells) showed light staining on both the scaffold surfaces.

The inflammatory response was evaluated in an in vivo subcutaneous model by implanting white and translucent 3D-printed scaffolds into the dorsum of Wistar rats. Histological samples from the white and translucent PLA scaffolds showed acute inflammation on day 7 and chronic inflammation on day 21, with giant cells present in both groups. By day 41, chronic inflammation had decreased, and blood vessel formation had increased, especially in the white scaffolds. Vascularization is considered a primary sign of tissue regeneration. These results align with those described by Abdul et al., in which subcutaneously implanted PLA scaffolds exhibited acute inflammation during the first week, with a reduction at 4 and 8 weeks, while blood vessel formation increased, which they interpreted as a sign of regeneration [54].

The importance of this study lies in its comprehensive approach, not only for evaluating the material (PLA) properties of 3D printed scaffolds but also for evaluating how the pigment in 3D-printed scaffolds may influence both material properties and their possible application in tissue engineering, with evaluations conducted in vitro and in vivo. Although no significant differences were found in the material properties, surface characteristics, or in vitro assays, the white 3D-printed scaffolds demonstrated better performance in terms of the inflammatory response, vascularization, and angiogenesis. It is well known that the regeneration response and degradation process can be influenced by the topographic characteristics of scaffolds, such as pore size, pore shape, and porosity [11,55–57]. The results indicate that the white-pigmented scaffold adhered more closely to the original 3D design. To further assess the influence of the 3D white-printed scaffold on regeneration, it is important to conduct in vitro degradation studies to determine whether the 3D white-printed scaffold can influence the regeneration response; researchers should perform in vitro degradation studies over an extended period to better simulate in vivo conditions and determine whether the pigment affects the material degradation process. In addition, evaluating both scaffolds in an in vivo bone model is crucial.

5. Conclusions

In conclusion, while both white and translucent PLA scaffolds exhibited similar material composition and surface characteristics, as well as comparable in vitro outcomes, notable differences were observed in their structural precision and biological response. The white PLA scaffold preserved its intended 3D architecture and pore definition more effectively, with a measured diameter of 9.15 ± 0.56 mm and width of 1.01 ± 0.2 mm, compared to the translucent scaffold, which measured 8.96 ± 0.85 mm in diameter and 0.97 ± 0.3 mm in width. Elemental analysis via EDS revealed that the translucent scaffold contained 61.37 ± 3.96 wt% carbon and 38.64 ± 3.95 wt% oxygen, while the white scaffold showed 56.28 ± 1.82 wt% carbon and 43.66 ± 1.92 wt% oxygen, suggesting minor compositional variation that may influence degradation and cell interaction. Importantly, the white scaffold elicited a more pronounced inflammatory response with visible signs of vascularization in vivo, likely due to better topographical cues from its preserved porous structure. These findings support the potential of white PLA scaffolds for enhanced biological integration; however, to draw definitive conclusions, researchers should include extended in vitro degradation assays (≥42 days) and

in vivo testing within a bone defect model to evaluate whether pigmentation or structural stability over time significantly affects performance in tissue regeneration contexts.

Acknowledgments

The authors would like to thank the Microscopy Center of the Institute of Physics at UNAM; Arch. Diego Armando Quiterio Vargas for sample preparation; PhD Samuel Tehuacanero Cuapa and MSc Jaqueline Cañetas Ortega for acquiring the scanning electron microscopy images; PhD Carolina Bohórquez Martínez for acquiring the Raman images; and PhD Luis Fernando Garrido García for acquiring the FTIR images. Data supporting the findings of this study are available upon request. This research was funded by DGAPA-UNAM-PAPIIT-IN218223, IN112022, and IN202924 projects.

Use of AI tools declaration

The authors declare they have used Artificial Intelligence (AI) tools in the creation of this article, such as Grammarly; a writing assistant that helps improve the writing by providing suggestions on grammar, spelling, punctuation, style, and tone.

Conflict of interest

The authors declare that they have no conflict of interest.

Author contributions

Mariana Nataly Carbajal Casique: Writing – original draft, Visualization, Investigation, Formal analysis, data curation, conceptualization: Writing Lucía Pérez-Sánchez review & editing, Supervision, Resources, Investigation, Conceptualization. Marco Antonio Álvarez-Pérez: Writing original draft, Investigation, Formal analysis, data curation, and funding acquisition. Gerardo Daniel Rayo-López Visualization, Investigation. Jorge-Alejandro Reyes-Esqueda: Investigation, Formal analysis, and funding acquisition. Francisco Marichi-Rodríguez Investigation, Formal analysis. Janeth Serrano-Bello: Writing review and editing, writing original draft, Visualization, Supervision, Resources, Project administration, funding acquisition, and conceptualization.

References

1. Lutzweiler G, Ndreu Halili A, Engin Vrana N (2020) The overview of porous, bioactive scaffolds as instructive biomaterials for tissue regeneration and their clinical translation. *Pharmaceutics* 12: 602. https://doi.org/10.3390/pharmaceutics12070602
2. Ikada Y (2006) Challenges in tissue engineering. *J R Soc Interface* 3: 589–601 https://doi.org/10.1098/rsif.2006.0124
3. Ko HS, Lee S, Lee D, et al. (2020) Mechanical properties and bioactivity of poly(Lactic acid) composites containing poly(glycolic acid) fiber and hydroxyapatite particles. *Nanomaterials* 11: 1–13. https://doi.org/10.3390/nano11010249

4. Messimer SL, Rocha Pereira T, Patterson AE, et al. (2019) Full-density fused deposition modeling dimensional error as a function of raster angle and build orientation: large dataset for eleven materials. *J Manufd MaterProcess* 3: 6. https://doi.org/10.3390/jmmp3010006
5. Wickramasinghe S, Do T, Tran P (2020) FDM-based 3D printing of polymer and associated composite: a review on mechanical properties, defects and treatments. *Polymers* 12: 1529. https://doi.org/10.3390/polym12071529
6. Howard D, Buttery LD, Shakesheff KM, et al. (2008) Tissue engineering: strategies, stem cells and scaffolds. *J Anat* 213: 66–72. https://doi.org/10.1111/j.1469-7580.2008.00878.x
7. Marin E (2023) History of dental biomaterials: biocompatibility, durability and still open challenges. *Herit Sci* 11: 207. https://doi.org/10.1186/s40494-023-01046-8
8. Raghunath J, Rollo J, Sales KM, et al. (2007) Biomaterials and scaffold design: key to tissue-engineering cartilage. *Biotechnol Appl Biochem* 46: 73–84. https://doi.org/10.1042/BA20060134
9. Tymrak BM, Kreiger M, Pearce JM (2014) Mechanical properties of components fabricated with open-source 3-D printers under realistic environmental conditions. *Mater Des* 58: 242–246. https://doi.org/10.1016/j.matdes.2014.02.038
10. Ranakoti L, Gangil B, Bhandari P, et al. (2023) Promising role of polylactic acid as an ingenious biomaterial in scaffolds, drug delivery, tissue engineering, and medical implants: research developments, and prospective applications. *Molecules* 28: 485. https://doi.org/10.3390/molecules28020485
11. Pérez-Sánchez L, Ortiz de la O MA, Álvarez-Pérez MA, et al. (2024) Standardization of 3D printing parameters to control the size and shape of pores in polylactic acid scaffolds. *MedComm Biomate Appl* 3: e74. https://doi.org/10.1002/mba2.74
12. Caramês JMM, Vieira FA, Caramês GB, et al. (2022) Guided bone regeneration in the edentulous atrophic maxilla using deproteinized bovine bone mineral (DBBM) combined with platelet-rich fibrin (PRF)—a prospective study. *J Clin Med* 11: 894. https://doi.org/10.3390/jcm11030894
13. Suniya NK, Verma AK (2023) A review on optimization of process parameters of fused deposition modeling. *Res Eng Struct Mater* 9: 631–659. https://doi.org/10.17515/resm2022.520ma0909
14. Zhang K, Fan Y, Dunne N, et al. (2018) Effect of microporosity on scaffolds for bone tissue engineering. *Regen Biomater* 5: 115–124. https://doi.org/10.1093/rb/rby001
15. Böttcher-Haberzeth S, Biedermann T, Reichmann E (2010) Tissue engineering of skin. *Burns* 36: 450–460. https://doi.org/10.1016/j.burns.2009.08.016
16. Zhao R, Yang R, Cooper PR, et al. (2018) Bone grafts and substitutes in dentistry: a review of current trends and developments. *Molecules* 26: 3007. https://doi.org/10.3390/molecules26103007
17. Farah S, Anderson DG, Langer R (2016) Physical and mechanical properties of PLA, and their functions in widespread applications — a comprehensive review. *Adv Drug Deliv Rev* 107: 367–392. https://doi.org/10.1016/j.addr.2016.06.012
18. O'Brien FJ (2011) Biomaterials & scaffolds for tissue engineering. *Mater Today* 14: 88–95. https://doi.org/10.1016/S1369-7021(11)70058-X
19. Soares JB, Finamor J, Silva FP, et al. (2018) Analysis of the influence of polylactic acid (PLA) colour on FDM 3D printing temperature and part finishing. *Rapid Prototyp* J 24: 1305–1316. https://doi.org/10.1108/RPJ-09-2017-0177

20. Valerga AP, Batista M, Salguero J, et al. (2018) Influence of PLA filament conditions on characteristics of FDM parts. *Materials* 11: 1322. https://doi.org/10.3390/ma11081322
21. Frunzaverde D, Cojocaru V, Ciubotariu CR, et al. (2022) The influence of the printing temperature and the filament color on the dimensional accuracy, tensile strength, and friction performance of FFF-printed PLA specimens. *Polymers* 14: 1978. https://doi.org/10.3390/polym14101978
22. Wittbrodt B, Pearce JM (2015) The effects of PLA color on material properties of 3-D printed components. *Addit Manuf* 8: 110–116. https://doi.org/10.1016/j.addma.2015.09.006
23. Joseph TM, Kallingal A, Suresh AM, et al. (2023) 3D printing of polylactic acid: recent advances and opportunities. *Int J Adv Manuf Technol* 125: 1015–1035. https://doi.org/10.1007/s00170-022-10795-y
24. Liao C, Li Y, Tjong SC (2020) Polyetheretherketone and its composites for bone replacement and regeneration. *Polymers* 12: 2858. https://doi.org/10.3390/polym12122858
25. Ramot Y, Haim-Zada M, Domb AJ, et al. (2016) Biocompatibility and safety of PLA and its copolymers. *Adv Drug Deliv Rev* 107: 153–162. https://doi.org/10.1016/j.addr.2016.03.012
26. Pavan Kalyan B, Kumar L (2022) 3D printing: applications in tissue engineering, medical devices, and drug delivery. *Aaps PharmSciTech* 23: 92. https://doi.org/10.1208/s12249-022-02242-8
27. Revati R, Abdul Majid MS, Ridzuan MJM, et al. (2017) Mechanical, thermal and morphological characterisation of 3D porous Pennisetum purpureum/PLA biocomposites scaffold. *Mater Sci Eng C* 75: 752–759. https://doi.org/10.1016/j.msec.2017.02.127
28. Fillingham Y, Jacobs J (2016) Bone grafts and their substitutes. *Bone Joint J* 98-B: 6–9. https://doi.org/10.1302/0301-620X.98B.36350
29. Beyerle A, Schulz H, Kissel T, et al. (2009) Screening strategy to avoid toxicological hazards of inhaled nanoparticles for drug delivery: the use of a-quartz and nano zinc oxide particles as benchmark. *J Phys Conf Ser* 151: 012034. https://doi.org/10.1088/1742-6596/151/1/012034
30. Gendviliene I, Simoliunas E, Alksne M, et al. (2021) Effect of extracellular matrix and dental pulp stem cells on bone regeneration with 3D printed PLA/HA composite scaffolds. *Eur Cell Mater* 41: 204–215. https://doi.org/10.22203/eCM.v041a15
31. Pant S, Thomas S, Loganathan S, et al. (2022) 3D bioprinted poly(lactic acid)/mesoporous bioactive glass based biomimetic scaffold with rapid apatite crystallization and in-vitro Cytocompatability for bone tissue engineering. *Int J Biol Macromol* 217: 979–997. https://doi.org/10.1016/j.ijbiomac.2022.07.202
32. Kubelka P, Munk F (1931) An article on optics of paint layers. *Tech Phys* 12: 593–601. https://doi.org/10.4236/jamp.2021.911188
33. Nanjundeswaraswamy TS, Divakar S (2021) Determination of sample size and sampling methods in applied research. *Proc Eng Sci* 3: 25–32. https://doi.org/10.24874/PES03.01.003
34. Onuma K, Watanabe M, Sasaki N (2024) The grimace scale: a useful tool for assessing pain in laboratory animals. *Exp Anim* 73 :234–245. https://doi.org/10.1538/expanim.24-0010
35. Liu YC, Lo GJ, Shyu VBH, et al. (2023) Surface modification of polylactic acid bioscaffold fabricated via 3D printing for craniofacial bone tissue engineering. *Int J Mol Sci* 24: 17410. https://doi.org/10.3390/ijms242417410

36. Zhang X, Chen JL, Xing F, et al. (2022) Three-dimensional printed polylactic acid and hydroxyapatite composite scaffold with urine-derived stem cells as a treatment for bone defects. *J Mater Sci Mater Med* 33: 71. https://doi.org/10.1007/s10856-022-06686-z
37. Valerga AP, Batista M, Puyana R, et al. (2017) Preliminary study of PLA wire colour effects on geometric characteristics of parts manufactured by FDM. *Procedia Manuf* 13: 924–931. https://doi.org/10.1016/j.promfg.2017.09.161
38. Beauson J, Schillani G, Van der Schueren L, et al. (2022) The effect of processing conditions and polymer crystallinity on the mechanical properties of unidirectional self-reinforced PLA composites. *Compos Part A Appl Sci Manuf* 152: 106668. https://doi.org/10.1016/j.compositesa.2021.106668
39. Mitchell MK, Hirt DE (2015) Degradation of PLA fibers at elevated temperature and humidity. *Polym Eng Sci* 55: 1652–1660. https://doi.org/10.1002/pen.24003
40. Laske S, Ziegler W, Kainer M, et al. (2015) Enhancing the temperature stability of PLA by compounding strategies. *Polym Eng Sci* 55: 2849–2858. https://doi.org/10.1002/pen.24176
41. Coppola B, Cappetti N, Di Maio L, et al. (2018) 3D printing of PLA/clay nanocomposites: influence of printing temperature on printed samples properties. *Materials* 11: 1947. https://doi.org/10.3390/ma11101947
42. Adamczyk A, Długoń E (2012) The FTIR studies of gels and thin films of Al_2O_3–TiO_2 and Al_2O_3–TiO_2–SiO_2 systems. *Spectrochim Acta A Mol Biomol Spectrosc* 89: 11–17. https://doi.org/10.1016/j.saa.2011.12.018
43. Wang L, Xie G, Mi X, et al. (2023) Surface-modified TiO_2@SiO_2 nanocomposites for enhanced dispersibility and optical performance to apply in the printing process as a pigment. *ACS Omega* 8: 20116–20124. https://doi.org/10.1021/acsomega.3c02679
44. Ciliveri S, Bandyopadhyay A (2022) Influence of strut-size and cell-size variations on porous Ti6Al4V structures for load-bearing implants. *J Mech Behav Biomed Mater* 126: 105023. https://doi.org/10.1016/j.jmbbm.2021.105023
45. Karageorgiou V, Kaplan D (2005) Porosity of 3D biomaterial scaffolds and osteogenesis. *Biomaterials* 26: 5474–5491. https://doi.org/10.1016/j.biomaterials.2005.02.002
46. Valenzuela-Villela KS, García-Casillas PE, Chapa-González C (2020) Progress of the 3D printing of medical devices. *Rev Mex Ing Biomed* 41: 151–66. https://doi.org/10.17488/RMIB.41.1.12
47. Zhao Y, Cai Y, Wang W, et al. (2025) Periosteum-bone inspired hierarchical scaffold with endogenous piezoelectricity for neuro-vascularized bone regeneration. *Bioact Mater* 44: 339–353. https://doi.org/10.1016/j.bioactmat.2024.10.020
48. Wang CY, Qin ZX, Wei Y, et al. (2023) The immunomodulatory effects of RNA-based biomaterials on bone regeneration. *Acta Biomater* 162: 32–43. https://doi.org/10.1016/j.actbio.2023.03.031
49. Song JH, Gu JT, Dang GP, et al. (2023) The immunomodulatory effects of DNA-conjugated collagen scaffolds on bone healing. *Chem Eng J* 474: 145318 https://doi.org/10.1016/j.cej.2023.145318
50. Amnael Orozco-Díaz C, Moorehead R, Reilly GC, et al. (2020) Characterization of a composite polylactic acid-hydroxyapatite 3D-printing filament for bone-regeneration. *Biomed Phys Eng Express* 6: 025007. https://doi.org/10.1088/2057-1976/ab73f8

51. Delgado-Calle J, Sañudo C, Sánchez-Verde L, et al. (2011) Epigenetic regulation of alkaline phosphatase in human cells of the osteoblastic lineage. *Bone* 49: 830–838. https://doi.org/10.1016/j.bone.2011.06.006
52. Bernar A, Gebetsberger JV, Bauer M, et al. (2022) Optimization of the alizarin red s assay by enhancing mineralization of osteoblasts. *Int J Mol Sci* 24: 723. https://doi.org/10.3390/ijms24010723
53. Wo J, Huang SS, Wu DY, et al. (2020) The integration of pore size and porosity distribution on Ti-6A1-4V scaffolds by 3D printing in the modulation of osteo-differentation. *J Appl Biomater Funct Mater* 18: 228080002093465. https://doi.org/10.1177/2280800020934652
54. Abdul Samat A, Abdul Hamid ZA, Jaafar M, et al. (2023) Investigation of the in vitro and in vivo biocompatibility of a three-dimensional printed thermoplastic polyurethane/polylactic acid blend for the development of tracheal scaffolds. *Bioengineering* 10: 394. https://doi.org/10.3390/bioengineering10040394
55. Moreira AC, Fernandes CP, de Oliveira MV, et al. (2021) The effect of pores and connections geometries on bone ingrowth into titanium scaffolds: an assessment based on 3D microCT images. *Biomed Mater* 16: 065010. https://doi.org/10.1088/1748-605X/ac246b
56. Pérez-Sánchez L, Ortiz de la O MA, González-Alva P, et al. (2021) In vivo study on bone response to 3D-printed constructs designed from microtomographic images. *J Mater Eng Perform* 30: 5005–5012. https://doi.org/10.1007/s11665-021-05585-8
57. Aronin CEP, Sadik KW, Lay AL, et al. (2009) Comparative effects of scaffold pore size, pore volume, and total void volume on cranial bone healing patterns using microsphere-based scaffolds. *J Biomed Mater Res A* 89: 632–641. https://doi.org/10.1002/jbm.a.32015

AIMS Press